Experimental Descriptors for the Synthesis of Multicationic Nickel Perovskite Nanoparticles for Oxygen Reduction

Francisco Gonell, Carlos M Sánchez-Sánchez, Vincent Vivier, Christel Laberty-Robert, David Portehault

To cite this version:

Francisco Gonell, Carlos M Sánchez-Sánchez, Vincent Vivier, Christel Laberty-Robert, David Portehault. Experimental Descriptors for the Synthesis of Multicationic Nickel Perovskite Nanoparticles for Oxygen Reduction. ACS Applied Nano Materials, 2020, 3 (8), pp.7482-7489. 10.1021/acsanm.0c01094 . hal-02912046

HAL Id: hal-02912046
https://hal.sorbonne-universite.fr/hal-02912046v1

Submitted on 1 Sep 2020

Experimental Descriptors for the Synthesis of Multicationic Nickel Perovskite Nanoparticles for Oxygen Reduction

*Francisco Gonell [a], Carlos M. Sánchez-Sánchez [b], Vincent Vivier [b], Christel Laberty-Robert [a], David Portehault[a,] **

[a] Sorbonne Université, CNRS, Laboratoire de Chimie de la Matière Condensée de Paris (CMCP), 4 place Jussieu, F-75005, Paris, France

[b] Sorbonne Université, CNRS, Laboratoire Interfaces et Systèmes Electrochimiques (LISE), 4 place Jussieu, F-75005, Paris, France

ABSTRACT

In many liquid-phase synthesis methods developed to produce nanomaterials, the key parameters governing the selective synthesis of solids and compounds are clearly identified, e.g. heat treatment profile, precursors solubility, pH, etc. Most of these well-understood approaches rely on relatively low temperature processes, below 400 °C, where conventional solvents are still stable. Interestingly, thermally stable inorganic molten salts enable to widen the temperature range for liquid-phase syntheses. They provide access to other families of crystalline solids requiring higher temperatures, as multicationic oxides. Nonetheless, the mechanisms that govern solid state formation and phase selection when different compounds compete are poorly understood. Herein, we report how experimental parameters, such as temperature, time, reaction medium composition and solvent oxo-basicity, enable to drive the synthesis mechanisms in molten salts towards nanoscaled multicationic oxides. We especially enlighten the phase-selective synthesis of pseudo-cubic perovskite $LaNiO_3$ and layered Ruddlesden-Popper phases La_2NiO_4 and $LaSrNiO_4$ at the nanoscale, by suggesting that the oxidation state of the metallic precursor plays a key role in the reaction pathway. This allows designing electrocatalysts for oxygen reduction reaction.

KEYWORDS. perovskite, layered materials, nickel oxide, oxygen reduction reaction, molten salts, synthesis mechanism.

INTRODUCTION

In the last decades, bottom-up nanomaterials synthesis has delivered exciting properties, with a plethora of nanoparticles accessible through solution chemistry, mostly in water or organic solvents. These liquids limit the synthesis temperature up to 350-400 °C. In this temperature range, metallic and ionic solids are easily crystallized. On the opposite, solids bearing a strong covalence character exhibit low crystallinity and even an amorphous character when they are prepared by liquid-phase synthesis. Indeed, such solids require a high temperature to overcome the energy barrier of crystallization, which includes reorganization of directional and strong bonds into the solid. Such high temperatures are energetically costly and trigger large crystal growth, hence inhibiting our ability to synthesize individualized nanoparticles.

This limit can be overcome by performing nanoparticles synthesis in molten salts.[1] These liquid media are especially suited for high temperature syntheses (generally up to 1000 °C),[1,2] because they are thermally stable, exhibit low vapor pressure and provide liquid media for the synthesis of nanoparticles with an increased reaction rate compared to solid-state processes. These enhanced kinetics result in a decrease in the grain size. Molten salts are then ideal to synthesize solids that need harsh conditions to crystallize through solid-state processes. Other advantages of molten salts encompass their low cost, low environmental impact and easy implementation at the large scale, as shown by their current industrial applications.[3] Molten salts have delivered materials previously not available at the nanoscale such as some multicationic oxides,[4–6] borides,[7–9] carbides,[10] group VI semiconductors,[11] etc. Despite numerous examples showing the rich versatility of molten salts for synthesis, reports dealing with reaction mechanisms in these media are scarce. Mechanistic studies would allow better understanding of nanoparticles formation in molten salts, enable selective synthesis of solids, and further provide design rules towards nanomaterials with tuned properties.

The perovskite structure can accommodate various anions and cations and shows a high compositional versatility to address various application fields.[12–15] This diversity is reflected into related materials such as Ruddlesden-Popper phases (RPs) with stoichiometry $A_{n+1}B_nO_{3n+1}$ (or $(AO)(ABO_3)_n$, n=1, 2…). RPs are built on *n* ABO_3 perovskite layers alternating with a AO rock-salt layer. Their transport properties are characteristic of two-dimensional materials.[16] AO layers and oxygen non-stoichiometry provide additional oxygen ion transport compared to the cubic perovskite structure. Nickel-based perovskites exhibit structural and compositional versatility, adjustable nickel oxidation state, ionic and/or electronic conductivity that make these materials widely studied for spintronics,[17] as redox catalysts in NO_x elimination,[18] and as electrocatalysts of the oxygen reduction reaction[19,20] in cathodes of Li–O_2 batteries[21,22] and solid oxide fuel cells.[23–25]

Nickel-based perovskites have been produced through solid–state synthesis above 1000 °C, yielding large crystals with uncontrolled morphology.[20] Sol-gel pathways have also been explored to produce materials with smaller crystal size. Yet, the thermal post-treatment required for crystallization hinders size and morphology control, and delivers crystals with large amounts of defects that limit charge transport. Molten salts are then promising media for lowering the synthesis temperature of nickel-based perovskites, to achieve smaller and more crystallized nanoparticles for tuning catalytic properties.

In this work, we demonstrate that a careful choice of the synthesis media and reaction conditions enables the production of $LaNiO_3$, La_2NiO_4 and $SrLaNiO_4$ nanoparticles through molten salts synthesis (**Scheme 1**). The synthesis mechanisms are studied to highlight the parameters governing the formation of nanoscaled multicationic oxides with controlled crystal structure. We then show that controlling the adequate synthesis parameters enables to tune the electrocatalytic activity of nickel-based perovskites for the oxygen reduction reaction (ORR) in alkaline solution.

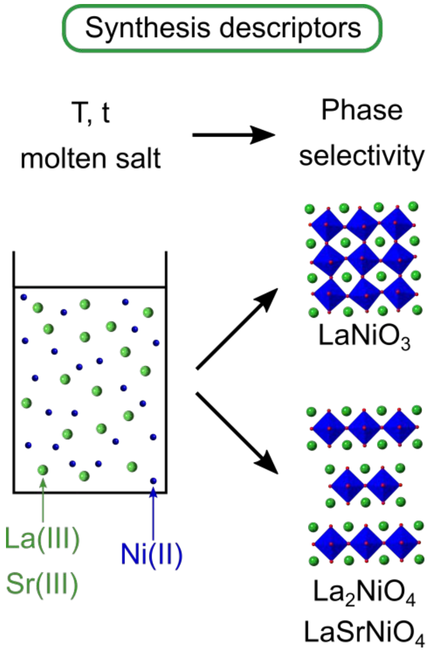

Scheme 1. Schematic representation of selective molten salt syntheses of Ni perovskites.

EXPERIMENTAL SECTION

Synthesis. All reagents were purchased from Sigma–Aldrich, otherwise written, and used as received without further purification. The amounts of precursors used in each synthesis are the following: Pseudo–cubic *$LaNiO_3$* synthesis: 6.5 mmol of $Ni(NO_3)_2{\cdot}6H_2O$, 6.5 mmol of $La(NO_3)_3{\cdot}6H_2O$, and 65 mmol of KNO_3 or 95 mmol of $NaNO_2$. Layered *La_2NiO_4* synthesis: 6.5 mmol of $Ni(NO_3)_2{\cdot}6H_2O$, 13 mmol of $La(NO_3)_3{\cdot}6H_2O$, and 65 mmol of KNO_3 or 95 mmol of $NaNO_2$. Layered *$LaSrNiO_4$* synthesis: 6.5 mmol of $Ni(NO_3)_2{\cdot}6H_2O$, 6.5 mmol of $La(NO_3)_3{\cdot}6H_2O$, 6.5 mmol of $Sr(NO_3)_2$ and 95.2 mmol of $NaNO_2$.

For each synthesis, the reagents were mixed with a few drops of ethanol, milled by using a Retsch MM400 ball miller with 50 mL stainless steel bowls filled with one ball. The resulting powder was dried under vacuum at 40 °C overnight. 2.5 g of each mixture was introduced in an alumina crucible and treated in a preheated oven at the corresponding temperature and time discussed in this work. Then, the reaction was quenched at room temperature by removing the crucible from the oven. The resulting black powder was washed by centrifugation with deionized water several times and dried under vacuum at room temperature overnight.

Seeded syntheses were performed to convert previous synthesized particles (seeds) into other perovskites: *$LaNiO_3$*: 0.25 g of La_2NiO_4, 0.6 mmol of $Ni(NO_3)_2{\cdot}6H_2O$ and 2.5 g of $NaNO_2$ were milled in an agate mortar and dried overnight at 40 °C under vacuum. This mixture was introduced in an alumina crucible and treated at several temperatures and times. *La_2NiO_4*: 0.25 g of $LaNiO_3$, 0.1 mmol of $La(NO_3)_3{\cdot}6H_2O$ and 2.5 g of $NaNO_2$ were milled in an agate mortar and dried overnight at 40 °C under vacuum. This mixture was introduced in an alumina crucible and treated at 800 °C for 0.5 hours. *$LaSrNiO_4$*: 0.25 g of $LaNiO_3$ or 0.41 g of La_2NiO_4, 0.1 mmol of $Sr(NO_3)_2$ and 2.5 g of $NaNO_2$ were milled in an agate mortar and dried overnight at 40 °C under vacuum. This mixture was introduced in an alumina crucible and treated at 800 °C. After 1 hour, all reaction media were quenched at room temperature, washed with deionized water several times and dried at room temperature under vacuum overnight.

Stability tests of the preformed materials in the reaction media, so-called “blank experiments” were performed with 0.25 g of the previously synthesized material, which was mixed with 2.5 g of $NaNO_2$ and milled in an agate mortar, then dried overnight at 40 °C under vacuum. This mixture was introduced in an alumina crucible and treated at the same temperature and time required for obtaining the targeted material (optimal conditions previously studied). Then, the synthesis media was quenched at room temperature and the as-synthesized material was washed with deionized water several times and dried at room temperature under vacuum overnight.

Characterization. Powder X–ray Diffraction (XRD) was performed on a Bruker D8 advance diffractometer equipped with a Cu Kα source. High resolution transmission electron microscopy (HRTEM) was carried out on a JEOL JEM2100Plus LaB_6 working at an accelerating voltage of 200 kV and field–emission scanning electron microscopy (SEM) on a Hitachi SU–70 microscope. XRD and electron diffraction patterns were indexed along the 00-033-0711, 00-034-0314, 04-007-0158 references from the PDF-4 database for $LaNiO_3$, La_2NiO_4, $LaSrNiO_4$, respectively. The atomic composition was measured by inductively coupled plasma optical emission spectrometry (ICP–OES) on a Varian Vista analyzer. The surface area was calculated from the adsorption branch of the N_2 sorption isotherm according to the BET method at 77 K using an ASAP 2010 equipment. Prior to sorption measurements, the powders were degassed at 300 °C for 4h.

The electrocatalytic properties were studied through a three-electrode setup, using a rotating disk electrode (RDE) made of glassy carbon as working electrode, a Pt wire as a counter electrode and an Ag/AgCl electrode as reference connected to a VPS Biologic potentiostat. As previously described,[26] a conductive ink containing the electrocatalyst (10 mg), black carbon (10 mg) and Nafion (435 μL) in ethanol (10 mL) was deposited on the polished glassy carbon (0.07 cm^2) of the RDE after sonification for 1 hour and then dried for 1 hour. 10 μL were deposited for performing cyclic voltammetry (CV) and lower amounts (2 μL) of the ink were used in order to see the catalyst deactivation during chronopotentiometry (current density: 0.5 mA $cm^{-2}{}_{disk}$). For comparison with benchmark catalys a ink with 20 % Pt/C (Alfa Aesar) was prepared using 12.5 mg of the material and the same amounts of EtOH and Nafion-117 as before. 1.5 µL of this ink was deposited on the GC electrode for performing the CV. The films were hydrated with one drop of 0.1 M KOH electrolyte during 30 min before the experiments.All the measurements were performed in O_2-saturated electrolyte at a 10 mV s^{-1} scan rate and a rotation rate of 1600 rpm. Each experiment was repeated 3 times to ensure reproducibility. Especially, the Koutecky-Levich analysis was performed for each sample on three different electrodes. The number of electrons exchanged was evaluated by averaging the two CV branches for each measurement. The numbers of electrons calculated for three different electrodes were then averaged and the different measurements enabled to evaluate the uncertainty at ±0.2 for each sample.

RESULTS AND DISCUSSION

The synthesis of $LaNiO_3$ and La_2NiO_4 was performed using metal nitrates (La(**III**) and Ni(**II**)) of varying ratios. KNO_3 was used as solvent to dissolve metal nitrates and to efficiently supply oxygen for the synthesis of perovskites.[4,27] The powder X–ray diffraction (XRD) patterns for the $LaNiO_3$ system (**Figure S1**) indicate that high temperature (800 °C) treatments and long reaction times (6 hours) are needed to obtain pure $LaNiO_3$. When the ratio of La and Ni reagents is adjusted to target La_2NiO_4, even prolonged heating at 800 °C for 14 h yields $LaNiO_3$ as the major product with a small amount of La_2NiO_4 (**Figure S2**). The results suggest that in KNO_3, the reagents are not sufficiently reactive to yield $LaNiO_3$ below 800 °C and to form single-phase La_2NiO_4. We then investigated a solvent prone to increase the reactivity of the initial metal salts by acting as a better O^{2-} source.

$NaNO_2$ is a good candidate thanks to its high oxo-basicity.[28] $NaNO_2$ has been efficiently used as synthesis medium for several systems including ZrO_2,[28–30] MgO,[31] $La_{0.5}Sr_{1.5}MnO_4$.[26] Indeed, the reactivity of Ni(II) and La(III) nitrates drastically increases in $NaNO_2$ (**Figure 1a**). $NaNO_2$ yields a mixture of $LaNiO_3$ and La_2NiO_4 at 600 °C (**Figure 1a**), while $LaNiO_3$ could not be detected in KNO_3 in similar conditions (**Figure S1**). The proportion of $LaNiO_3$ increases with the reaction time, as shown by the increased relative intensity of the corresponding XRD peaks. Minor amounts of NiO are also detected at 600 °C (**Figure 1a**). The crystal size calculated from XRD for $LaNiO_3$ obtained at

600 °C/8 h is 33 nm and the surface area is 9 m^2 g^{-1} according to N_2 sorption. Inductively coupled plasma (ICP) analysis confirmed the expected La:Ni ratio 1:1.

Scanning (SEM) and transmission (TEM) electron microscopies show that $LaNiO_3$ is composed of well faceted truncated cubes with an average size of 100 nm (**Figure 1b–d**). Smaller 20 nm particles are also visible in these images. Energy dispersive X–ray (EDX) analysis indicates only the presence of Ni and O in these particles, in agreement with high resolution TEM (HRTEM, **Figure S3**) indicating the NiO structure, as powder XRD (**Figure 1a**). Focusing on the 100 nm particles (**Figure 1e**), the selected area electron diffraction (SAED) pattern can be indexed over $LaNiO_3$ structure. Interestingly, seemingly aggregated particles show a single crystal–like pattern, indicating highly oriented crystals. **Figure 1f** shows a HRTEM micrograph of a particle

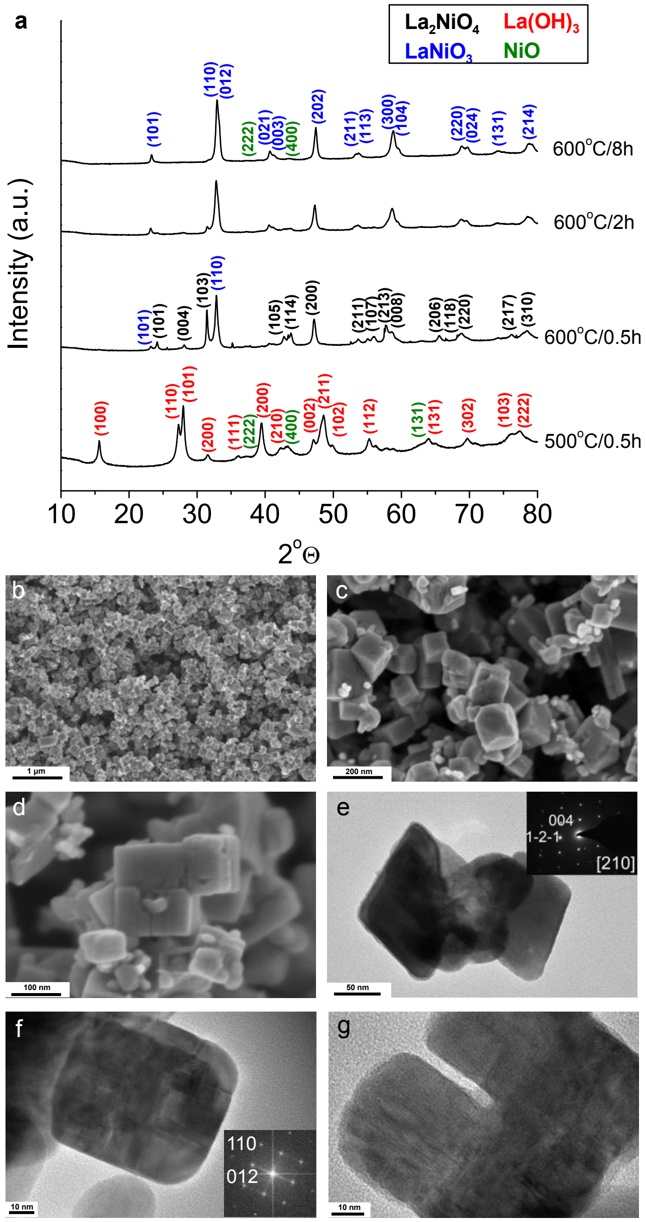

Figure 1. (a) XRD diagrams of the powders obtained at different temperatures and reaction times when targeting $LaNiO_3$ in $NaNO_2$. Electron microscopy study of $LaNiO_3$ (600 °C/8h): (b–d) SEM and (e) TEM images (inset shows the corresponding SAED

pattern of the particles ensemble. (f, g) HRTEM image (inset shows the corresponding FFT). The SAED and FFT are indexed along the $LaNiO_3$ structure.

of 80 nm diameter, which can again be fully indexed on the $LaNiO_3$ structure. The material is then composed of a majority of ~100 nm $LaNiO_3$ cubes with small amounts of 20 nm NiO particles. The $LaNiO_3$ particle size measured by electron microscopy is larger than the one calculated by XRD. This discrepancy might originate from the ~100 nm particles (**Figure 1d** and **1g**) being formed by aggregation of smaller cubic particles. ~30 nm cubic particles are indeed perfectly oriented in respect to each other within large cubes. The defects at the grain boundaries may limit the lattice coherence, yielding small XRD crystal size, even if the primary grains are iso-oriented as shown by SAED and HRTEM.

When the La:Ni ratio is increased in order to obtain the RP phase La_2NiO_4, the behavior of the reaction medium changes completely. At 600 °C, the product is a mixture of $La(OH)_3$ and La_2NiO_4 (**Figure 2a**). The content of the RP phase increases with the temperature up to 800 °C. When the reaction time is increased from 0.5 h to 2 h, the layered phase disappears at the benefit of hydroxides. Then, in the optimal temperature/time conditions (800 °C/0.5 h), the La:Ni ratio was adjusted by decreasing the La concentration and keeping constant the Ni content, in order to avoid the formation of $La(OH)_3$ impurity. For the nominal ratio La:Ni = 1.8:1, the $La(OH)_3$ content is minimized (**Figure S4**). The material then consists in La_2NiO_4 with minor amounts of lanthanum hydroxide. The La_2NiO_4 crystal size calculated from XRD patterns is 76 nm and the surface area evaluated by N_2 adsorption is 9 m^2 g^{-1}. The composition evaluated by ICP analysis matches La_2NiO_4. SEM and TEM indicate that La_2NiO_4 is composed of faceted 60 nm nanoparticles (**Figure 2b–e**), in agreement with the Scherrer crystallite size. SAED shows that the material is composed by single crystal nanoparticles randomly oriented (**Figure 2c**). Some grain boundaries can also be observed, showing iso–oriented crystals (**Figure 2d and e**).

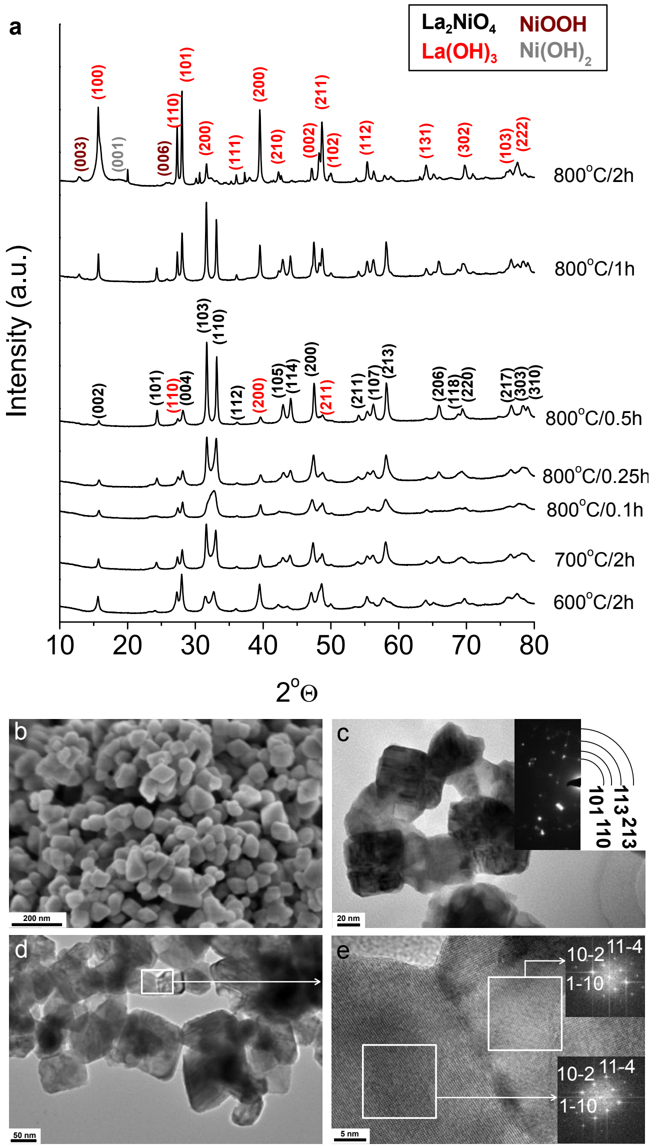

Figure 2. (a) XRD diagrams of the powders obtained at different temperatures and reaction times when targeting La_2NiO_4 in $NaNO_2$. Electron microscopy images of La_2NiO_4 (800 °C/0.5h) (b) SEM and (c and d) low magnification TEM images (inset in c shows the corresponding SAED pattern indexed along the La_2NiO_4 structure). (e) HRTEM image

(insets shows the corresponding FFTs of each area in the squares. They are indexed along the La_2NiO_4 structure).

Compared to KNO_3, the use of $NaNO_2$ as solvent enables a 200 °C decrease of the reaction temperature for obtaining the pseudo-cubic perovskite. On the other side, the selectivity towards the layered perovskite structure drastically increases, so that the pseudo-cubic phase could not be detected in the whole synthesis temperature range. The higher Lux-Flood basicity that NO_2^- shows compared to NO_3^- indicates its larger propensity to deliver O^{2-} in the synthesis media.[28] Indeed the dissociation constant to oxide anions is 10^{10} higher for nitrites than for nitrates.[28] The increase in the O^{2-} concentration, namely the oxo-basicity, may equalize cations reactivity, as it is reported in aqueous media with Brønsted basicity at high pH.[32] Such a behavior is also well documented in non-hydrolytic sol-gel synthesis of titanate perovskites,[33] which results from the reactivity of the different cations being very similar in e.g. benzylic alcool.[33] Hence, the increase in oxo-basicity should result in the common incorporation of different cations in the same compound. The higher oxo-basicity of molten nitrites also drives phase selectivity to oxygen-rich solids, hence favoring the RP phase versus the pseudo-cubic perovskite.

The high versatility of molten salt syntheses allowed expanding the range of layered perovskites by replacing lanthanum with strontium. **Figure 3a** shows the evolution of the crystalline structure as a function of the synthesis temperature and time towards $LaSrNiO_4$. At 600 °C, the XRD peaks can be assigned to La_2NiO_4, which is confirmed by EDX that does not detects Sr. By increasing the temperature, Sr could be incorporated in the material (La_2NiO_4 and $Sr_4Ni_3O_9$ at 700 °C). At 800 °C and 0.5 h, the peaks corresponding to (103) and (110) planes of the layered perovskite structure show a shoulder, which indicates the presence of La_2NiO_4 and $LaSrNiO_4$. After 1 h at 800 °C, La_2NiO_4 disappears and $LaSrNiO_4$ remains the major product. The XRD crystal size of $LaSrNiO_4$ is 49 nm, with a BET surface area of 13 m^2 g^{-1} and a well faceted

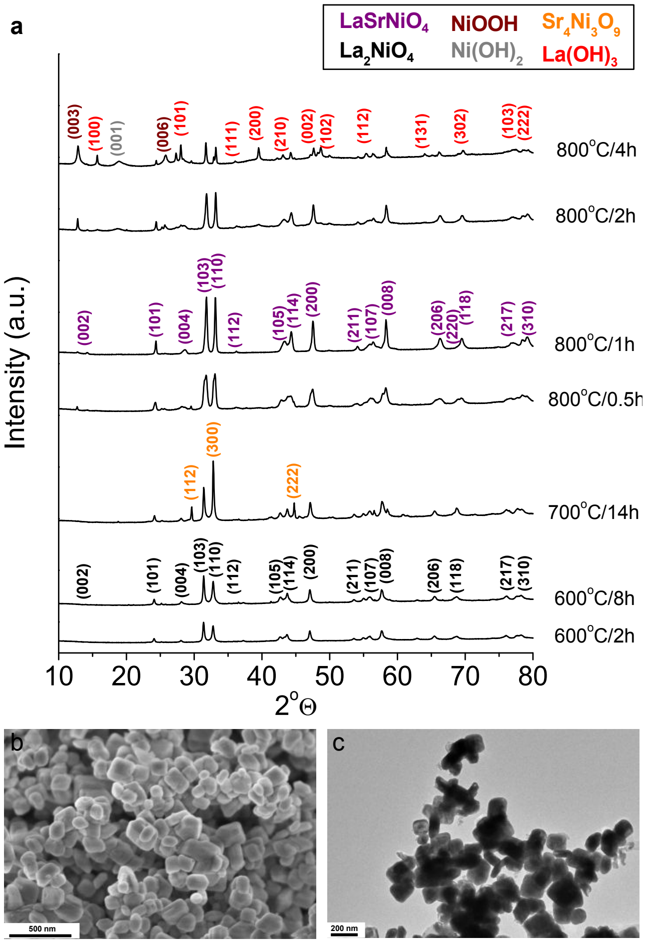

Figure 3. (a) XRD diagrams of the powders obtained at different temperatures and reaction times when targeting $LaSrNiO_4$ in $NaNO_2$. (b) SEM and (c) TEM micrographs of $LaSrNiO_4$ obtained at 800 °C/1h.

morphology of platelets of 100–200 nm basal face and 50 nm thickness (**Figure 3b** and **c**). If the synthesis time is prolonged beyond 1 h, the XRD peaks of the layered compound disappear, showing that the RP phase decomposes. The final product obtained after washing is composed of several single cation hydroxides. No significant change in the XRD patterns (**Figure S5**), morphology (**Figure S6a** and **b**) and composition (**Table S1**) was observed when the content of strontium in the reaction medium was increased. When no strontium was introduced, the product was a mixture of different single cation (oxy)hydroxides. This observation highlights the importance of strontium to stabilize the Ruddlesden-Popper structure, in good agreement with the decomposition of La_2NiO_4 at 800 °C/1h (**Figure 3a**). A slight shift of (103) and (110) planes towards lower angles is observed when the Sr content decreases, in agreement with the decreasing amount of strontium in the materials (**Table S1**) and the expected increase of the lattice parameters in relation with the ionic radii of La(III) (1.15 Å) and Sr(II) (1.13 Å). The material with the lowest strontium content (La:Ni:Sr 1:1:0.2) shows particle a size around 70 nm very similar that the one when targeting La_2NiO_4 **(Figure S6c** and **d).**

A common feature is observed for the pathways of crystallization in all the syntheses reported above. In the two systems $LaNiO_3$ and $LaSrNiO_4$, low temperatures and short reaction times result La_2NiO_4 as an intermediate product. Such behavior can be explained on the basis of nickel oxidation state (OS). The nickel precursor used in the synthesis is nickel(II) species, as in the intermediate phase La_2NiO_4. Hence, the two different reaction media evolve through a first step involving no redox processes, but only the basicity of the solvent: the first step consists in the evolution through constant oxidation state Ni(II). Then, in a second step, nickel appears to be oxidized to Ni(III) and yield $LaNiO_3$ and $LaSrNiO_4$, depending on the medium composition. Hence, we suggest that the nickel oxidation state drives phase selectivity during the synthesis (**Scheme 1**).

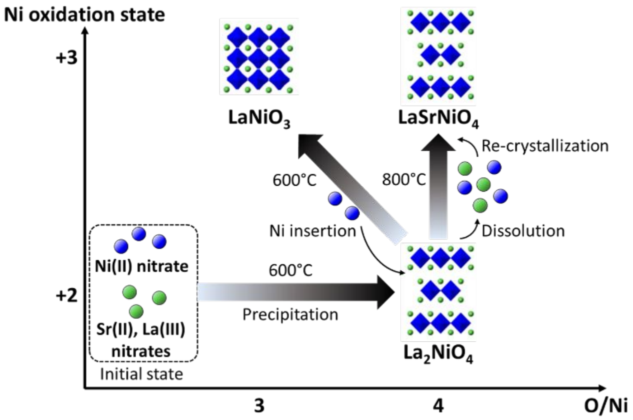

Scheme 2. Proposed mechanisms involved in the synthesis of nickel-based perovskites.

If the nickel oxidation state drives the crystallization pathways of nickel-based perovskites in $NaNO_2$, the mechanisms of transformation from the intermediate phase La_2NiO_4 to the final compounds in molten $NaNO_2$ require further discussion. In order to shed light on this aspect, syntheses have been performed by using preformed perovskite particles in the presence (seeded synthesis) and in the absence (blank synthesis) of the metal salt precursor required to reach the adequate stoichiometry in the final product.

Treating La_2NiO_4 in molten $NaNO_2$ without metal salt, the structure is stable in that solvent at 600 °C for 8 h, the conditions of formation of $LaNiO_3$ (**Figures 1** and **SI7a**). The particle size however increases to 100 nm (**Figure S8**), which is probably caused by severe heat-treatment conditions. When the stoichiometric amount of $Ni(NO_3)_2{\cdot}6H_2O$ is introduced in order to reach $LaNiO_3$, the phase evolution observed (**Figure S7b** and **c**) is similar to the direct synthesis of $LaNiO_3$ from the metal salts. When the temperature of synthesis is raised to 800 °C, the perovskite structure decomposes, yielding (oxy)hydroxides (**Figure S7d**). These species are observed after washing the $NaNO_2$ salt with water. They most probably indicate dissolution of the perovskite into molten $NaNO_2$.[34] TEM micrographs (**Figure S9**, **S10** and **S11**) of the intermediate sample formed from the La_2NiO_4 seeds (600 °C/1h) show particles of 100–200 nm surrounded by nanoparticles of 50 nm, and smaller nanoparticles of 5 nm. The elemental distribution of this intermediate state was mapped by Scanning TEM coupled to Energy Dispersive X-ray Spectroscopy (STEM–EDS, **Figures S10** and **S11**). The 100–200 nm and 50 nm cubes are composed by La, Ni and O homogeneously distributed, while smaller 5 nm particles are made of Ni and O. HRTEM (**Figure S12**) shows that the crystal lattice of the 100-200 nm cubic particles corresponds to the $LaNiO_3$ structure, in agreement with the colocation of La, Ni and O. The 50 nm particles show lattice fringes in agreement with the La_2NiO_4 structure (**Figure S13**), while the ~5 nm particles at the surface of the larger ones are amorphous and composed by Ni and O. Finally, the sample obtained after 8 h at 600 °C (**Figure S14**) shows the same 100 nm well faceted cubic morphology as in the original synthesis from the La(III) and Ni(II) salts.

The stability of La_2NiO_4 particles in molten $NaNO_2$ in the conditions of formation of $LaNiO_3$ (temperature, time), and their morphological, structural and compositional evolution when reacted with nickel (II) nitrate suggest that the formation of $LaNiO_3$ goes through insertion of the dissolved nickel(II) species into the layered RP La_2NiO_4 structure (**Scheme 1**). This cation insertion may occur through a topochemical transformation, as observed for several layered perovskites.[5] A hint of such a reaction mechanism may be found in the persistence of the morphology of the La_2NiO_4 particles in the final product. In the present case, the $LaNiO_3$ product from the seeded synthesis is obtained as particles of c.a. 100 nm. During the transformation, one can distinguish smaller building blocks (**Figure S12**) also observed in the direct synthesis from the metal salts (**Figure 1g**). These blocks may be originally the ca. 50 nm La_2NiO_4 nanoparticles that have reacted and coalesced.

Blank and seeded syntheses from $LaNiO_3$ and La_2NiO_4 particles in the same conditions of synthesis of La_2NiO_4 and $LaSrNiO_4$, respectively, yield mixtures of (oxy)hydroxides after washing (**Figure S15** and **S16**). Therefore, the precursor particles were decomposed and the cations were dissolved in the reaction medium. This observation suggests that the synthesis goes through a dissolution-reprecipitation mechanism (**Scheme 1**).[32] The difference in the synthesis mechanism toward $LaNiO_3$ on one side, La_2NiO_4 and $LaSrNiO_4$ on the other side, going through topochemical transformation and dissolution-reprecipitation, respectively, can be explained in terms of synthesis temperatures. Indeed, it is possible to hypothesize that at 600 °C, the temperature may not be sufficient to trigger dissolution of intermediate La_2NiO_4, so that its transformation to pseudo-cubic $LaNiO_3$ occurs within the La_2NiO_4 particles. At higher temperature, 800 °C, the dissolution of intermediate phases is increased and enables crystallization by dissolution followed by re-precipitation (**Scheme 1**).

The diversity of nanostructured ligand-free nickel-based perovskites, with lack of defects, obtained through molten salts synthesis provides a unique opportunity to study the influence of the crystal structure of perovskite-related oxides in the oxygen reduction reaction (ORR). In order to study these properties, a conductive ink was prepared with each catalyst and deposited on a rotating disk electrode (RDE), as described in the experimental section. The cyclic voltammograms (CVs) were recorded using a three electrode setup, at a rotating speed of 1600 rpm, in O_2 saturated 0.1M KOH. Note that the possible impurities detected by XRD (lanthanum hydroxide, nickel oxide) are not active[35] in ORR so that the electrocatalytic activities measured originate from the perovskite materials.

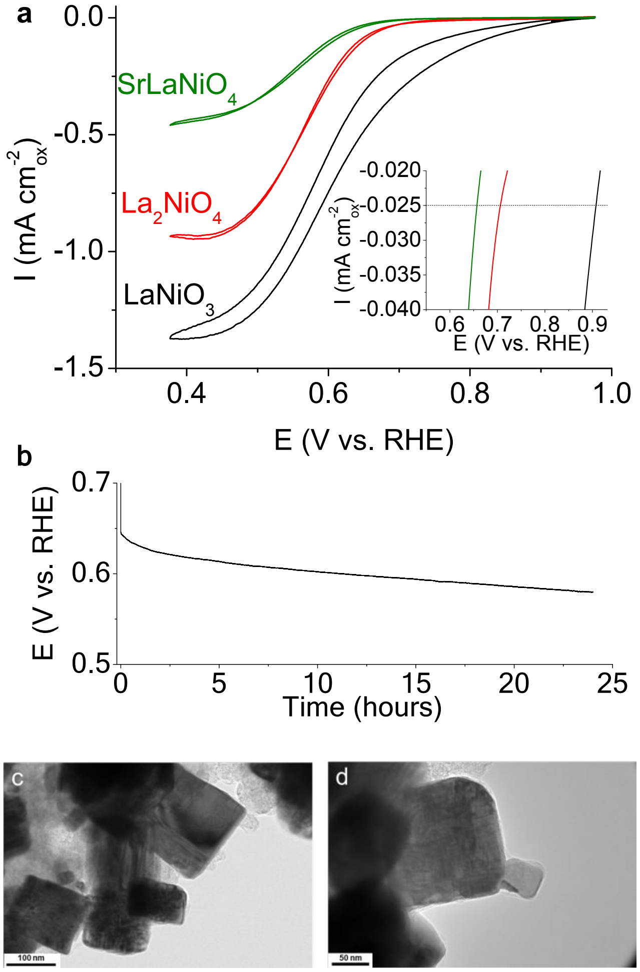

Figure 4. (a) Cyclic voltammograms in ORR conditions (oxide surface-normalized specific activity, O_2-saturated 0.1 M KOH electrolyte) of (a) $LaNiO_3$, La_2NiO_4 and $SrLaNiO_4$ at 1600 rpm. The inset shows a zoom of the onset region. (b) Chronopotentiometry curve of $LaNiO_3$ at 0.5 mA cm$^{-2}{}_{disk}$, (c and d) TEM images of $LaNiO_3$ after chronopotentiometry. The light contrast particles of 50 nm in (c) are carbon black particles used as conductive additive.

The oxide surface area-normalized cyclic voltammograms (CVs) (**Figure 4a, Figure S17**) show that $LaNiO_3$ is the most active material followed by La_2NiO_4 and $SrLaNiO_4$ with a potential at 25 μA cm^{-2}_{ox} of 0.91, 0.71 and 0.66 V/RHE, respectively. Tafel slopes (**Figure S18**) are 56, 208 and 152 mV·dec^{-1} for $LaNiO_3$, La_2NiO_4 and $LaSrNiO_4$ respectively, in good agreement with previous works[36] and with the overpotentials described above, where the most active materials show lower slopes. The values obtained for $LaNiO_3$ are in agreement with the values previously reported on bulk materials,[19,37] thus highlighting the high crystallinity of the nanoparticles. Noteworthy, crystallization and significant electrocatalytic activity are triggered by syntheses in molten salts at lower temperature than by using sol-gel and solid-state derived methodologies. $LaNiO_3$ shows a half-wave potential of 0.61 V vs RHE. This value is lower than for the benchmark Pt/C electrocatalyst (**Figure S19)** but is comparable to other active perovskites.[38] As other perovskite electrocatalysts, the nickelates reported herein have the advantage of not containing any precious metal.

The order of activity $LaNiO_3$ > La_2NiO_4 > $SrLaNiO_4$ can be explained by the filling of the Ni 3d orbitals.[19] According to Shao- Horn *et al.*[19] perovskites bearing B-site transition metals with configurations d^4 or d^7 show the highest ORR activity because e_g degenerated orbitals hold one electron for optimal O_2 adsorption.[19] The d^7 configuration of nickel in $LaNi^{III}O_3$ then explains its highest activity. On the contrary, La_2NiO_4 exhibits a d^8 configuration with lower activity. $SrLaNi^{III}O_4$ seems to deviate from the d^4/d^7 rule as it shows the lowest activity despite a d^7 configuration. Surface termination with Sr^{2+} and La^{3+} cations instead of catalytically active nickel may explain this discrepancy. The number of electrons involved in the ORR according to the Koutecky-Levich analysis (**Figures S20**, **S21** and **S22**) is 3.5, 3.4 and 3.0 (±0.2) electrons per O_2 for $LaNiO_3$, La_2NiO_4 and $SrLaNiO_4$ respectively, suggesting a mixture of 4- and 2- electron mechanisms. The stability of $LaNiO_3$ during ORR was studied with chronopotentiometry (**Figure 4b**), showing only a slight deactivation during 24 hours operation. The potential required for reaching a current density of 0.5 mA $cm^{-2}{}_{disk}$ evolves from -0.65 to -0.58 V/RHE. This is reflected in the downward shift of the CVs from the initial state to the final state (**Figure S23**). This slight decay may arise from the partial reduction of Ni(**III**) to less active Ni(II) under the reductive conditions applied during the stability test. HRTEM (**Figure 4c-d**) shows no significant change of the well faceted cubic morphology after chronopotentiometry. In addition, STEM-EDS mapping for $LaNiO_3$ after chronopotentiometry shows homogeneous Ni and La distribution (**Figure S24)**, while the atomic composition remains constant, according to EDS analysis. These data further support the stability of the $LaNiO_3$ particles under operation thanks to their high crystallinity.

CONCLUSION

In this work an accurate choice of the synthetic conditions (temperature, time and solvent oxo-basicity) in molten salts led to the selective synthesis of $LaNiO_3$, La_2NiO_4 and $LaSrNiO_4$ as new nanomaterials that are active electrocatalysts of the oxygen reduction reaction in alkaline media. Reaction intermediates were identified to shed light on the key parameters controlling the formation of nickel-based perovskites in molten salts. Nickel oxidation state governs the perovskite formation, through a common low oxidation state

Ni(II) intermediate (La_2NiO_4) formed from a Ni(II) salt precursor. The intermediate La_2NiO_4 phase then evolves to structures with higher Ni oxidation state depending on the composition of the reaction medium and on the temperature. Low temperatures (600 °C) favor a topochemical transformation where nickel species in solution are inserted into the reaction intermediate La_2NiO_4. At higher temperature, the energy input is high enough to trigger dissolution of the precursors promoting a dissolution-reprecipitation pathway.

These results highlight experimental descriptors that govern the formation of nanoparticles of multicationic oxides in molten salts media. We suggest that the oxidation state of the precursor determines the nature of the reaction intermediate, whose further evolution is driven by the composition of the medium and the temperature. These reaction rules should enable further design of synthesis protocols towards multicationic oxides at nanoscale and electrocatalysts for the oxygen reduction reaction and the oxygen evolution reaction.

ASSOCIATED CONTENT

Supporting Information.

The Supporting Information is available free of charge at

https://pubs.acs.org/doi/xxxxxxxxxxxx

Additional XRD, TEM, electrocataytic and ICP characterization (PDF).

AUTHOR INFORMATION

Corresponding Author

*E-mail: david.portehault@sorbonne-universite.fr

Funding Sources

The whole research program received financial support from Region Ile-de-France in the framework of the Domaine d’Intérêt Majeur DIM Nano-K and from the French national agency for research (ANR) with the project SALTYSPIN ANR-17-CE09-0005. DP and FG also acknowledge support from the Fondation Collège de France.

Notes

The authors declare no competing financial interest.

REFERENCES

(1) Liu, X.; Fechler, N.; Antonietti, M. Salt Melt Synthesis of Ceramics, Semiconductors and Carbon Nanostructures. *Chem. Soc. Rev.* **2013**, *42* (21), 8237–8265. https://doi.org/10.1039/c3cs60159e.

(2) Portehault, D.; Delacroix, S.; Gouget, G.; Grosjean, R.; Chan-Chang, T.-H.-C. Beyond the Compositional Threshold of Nanoparticle-Based Materials. *Acc. Chem. Res.* **2018**, *51*, 930–939. https://doi.org/10.1021/acs.accounts.7b00429.

(3) Carenco, S.; Portehault, D.; Boissière, C.; Mézailles, N.; Sanchez, C. Nanoscaled Metal Borides and Phosphides: Recent Developments and Perspectives. *Chem. Rev.* **2013**, *113*, 7981–8065. https://doi.org/10.1021/cr400020d.

(4) Thi N'Goc, H. Le; Mouafo, L. D. N.; Etrillard, C.; Torres-Pardo, A.; Dayen, J.-F.; Rano, S.; Rousse, G.; Laberty-Robert, C.; Calbet, J. G.; Drillon, M.; et al. Surface-Driven Magnetotransport in Perovskite Nanocrystals. *Adv. Mater.* **2017**, *29*,

1604745. https://doi.org/10.1002/adma.201604745.

(5) Li, L.; Deng, J.; Chen, J.; Xing, X. Topochemical Molten Salt Synthesis for Functional Perovskite Compounds. *Chem. Sci.* **2016**, *7* (2), 855–865. https://doi.org/10.1039/c5sc03521j.

(6) Liu, H.; Hu, C.; Wang, Z. L. Composite-Hydroxide-Mediated Approach for the Synthesis of Nanostructures of Complex Functional-Oxides. *Nano Lett.* **2006**, *6* (7), 1535–1540. https://doi.org/10.1021/nl061253e.

(7) Portehault, D.; Devi, S.; Beaunier, P.; Gervais, C.; Giordano, C.; Sanchez, C.; Antonietti, M. A General Solution Route toward Metal Boride Nanocrystals. *Angew. Chem. Int. Ed.* **2011**, *50* (14), 3262–3265. https://doi.org/10.1002/anie.201006810.

(8) Gouget, G.; Beaunier, P.; Portehault, D.; Sanchez, C. New Route toward Nanosized Crystalline Metal Borides with Tunable Stoichiometry and Variable Morphologies. *Faraday Discuss.* **2016**, *191*, 511–525.

(9) Gouget, G.; Debecker, D. P.; Kim, A.; Olivieri, G.; Gallet, J.-J.; Bournel, F.; Thomas, C.; Ersen, O.; Moldovan, S.; Sanchez, C.; et al. In Situ Solid-Gas Reactivity of Nanoscaled Metal Borides from Molten Salt Synthesis. *Inorg. Chem.* **2017**, *56*,

9225–9234.

(10) Liu, X.; Antonietti, M.; Giordano, C. Manipulation of Phase and Microstructure at Nanoscale for SiC in Molten Salt Synthesis. *Chem. Mater.* **2013**, *25* (10), 2021–2027. https://doi.org/10.1021/cm303727g.

(11) Liu, X.; Giordano, C.; Antonietti, M. A Molten-Salt Route for Synthesis of Si and Ge Nanoparticles: Chemical Reduction of Oxides by Electrons Solvated in Salt Melt. *J. Mater. Chem.* **2012**, *22* (12), 5454. https://doi.org/10.1039/c2jm15453f.

(12) Konstantakou, M.; Stergiopoulos, T. A Critical Review on Tin Halide Perovskite Solar Cells. *J. Mater. Chem. A* **2017**, *5* (23), 11518–11549. https://doi.org/10.1039/C7TA00929A.

(13) Hashim, S. S.; Somalu, M. R.; Loh, K. S.; Liu, S.; Zhou, W.; Sunarso, J. Perovskite-Based Proton Conducting Membranes for Hydrogen Separation: A Review. *Int. J. Hydrogen Energy* **2018**, *43* (32), 15281–15305. https://doi.org/10.1016/j.ijhydene.2018.06.045.

(14) Sunarso, J.; Hashim, S. S.; Zhu, N.; Zhou, W. Perovskite Oxides Applications in High Temperature Oxygen Separation, Solid Oxide Fuel Cell and Membrane

Reactor: A Review. *Prog. Energy Combust. Sci.* **2017**, *61*, 57–77. https://doi.org/10.1016/j.pecs.2017.03.003.

(15) Ansari, M. I. H.; Qurashi, A.; Nazeeruddin, M. K. Frontiers, Opportunities, and Challenges in Perovskite Solar Cells: A Critical Review. *J. Photochem. Photobiol. C Photochem. Rev.* **2018**, *35*, 1–24. https://doi.org/10.1016/j.jphotochemrev.2017.11.002.

(16) Lobanov, M. V.; Li, S.; Greenblatt, M. Structural, Magnetic, and Transport Properties of the Two Electron-Doped Ruddlesden−Popper Manganites Ca 3 - x Th x Mn 2 O 7. *Chem. Mater.* **2003**, *15* (6), 1302–1308. https://doi.org/10.1021/cm020470n.

(17) Demont, A.; Hébert, S.; Pelloquin, D.; Maignan, A. The Sr2.75Ce0.25Co2O7−δ Oxide, N=2 Member of the Ruddlesden–Popper Series: Structural and Magnetic Evolution Depending on Oxygen Stoichiometry. *J. Solid State Chem.* **2008**, *181* (6), 1314–1320. https://doi.org/10.1016/j.jssc.2008.02.023.

(18) Zhu, J.; Thomas, A. Perovskite-Type Mixed Oxides as Catalytic Material for NO Removal. *Appl. Catal. B Environ.* **2009**, *92* (3–4), 225–233.

https://doi.org/10.1016/j.apcatb.2009.08.008.

(19) Suntivich, J.; Gasteiger, H. a; Yabuuchi, N.; Nakanishi, H.; Goodenough, J. B.; Shao-Horn, Y. Design Principles for Oxygen-Reduction Activity on Perovskite Oxide Catalysts for Fuel Cells and Metal-Air Batteries. *Nat. Chem.* **2011**, *3* (7), 546–550. https://doi.org/10.1038/nchem.1069.

(20) Yu, J.; Sunarso, J.; Zhu, Y.; Xu, X.; Ran, R.; Zhou, W.; Shao, Z. Activity and Stability of Ruddlesden-Popper-Type Lan+1Nin O3n +1(n =1, 2, 3, and ∞) Electrocatalysts for Oxygen Reduction and Evolution Reactions in Alkaline Media. *Chem. - A Eur. J.* **2016**, *22*, 1–10. https://doi.org/10.1002/chem.201504279.

(21) Zhang, J.; Zhao, Y.; Zhao, X.; Liu, Z.; Chen, W. Porous Perovskite LaNiO3 Nanocubes as Cathode Catalysts for Li-O2 Batteries with Low Charge Potential. *Sci. Rep.* **2015**, *4* (1), 6005. https://doi.org/10.1038/srep06005.

(22) Wei, Z.; Cui, Y.; Huang, K.; Ouyang, J.; Wu, J.; Baker, A. P.; Zhang, X. Fabrication of La 2 NiO 4 Nanoparticles as an Efficient Bifunctional Cathode Catalyst for Rechargeable Lithium–Oxygen Batteries. *RSC Adv.* **2016**, *6* (21), 17430–17437. https://doi.org/10.1039/C5RA23053E.

(23) Pikalova, E. Y.; Bogdanovich, N. M.; Kolchugin, A. A.; Osinkin, D. A.; Bronin, D. I. Electrical and Electrochemical Properties of La2NiO4+δ-Based Cathodes in Contact with Ce0.8Sm0.2O2-δ Electrolyte. *Procedia Eng.* **2014**, *98*, 105–110. https://doi.org/10.1016/j.proeng.2014.12.495.

(24) Woolley, R. J.; Skinner, S. J. Functionally Graded Composite La 2 NiO 4+δ and La 4 Ni 3 O 10−δ Solid Oxide Fuel Cell Cathodes. *Solid State Ionics* **2014**, *255*, 1–5. https://doi.org/10.1016/j.ssi.2013.11.041.

(25) BOEHM, E.; BASSAT, J.; DORDOR, P.; MAUVY, F.; GRENIER, J.; STEVENS, P. Oxygen Diffusion and Transport Properties in Non-Stoichiometric LnNiO Oxides. *Solid State Ionics* **2005**, *176* (37–38), 2717–2725. https://doi.org/10.1016/j.ssi.2005.06.033.

(26) Gonell, F.; Sanchez-Sanchez, C. M.; Vivier, V.; Méthivier, C.; Laberty-Robert, C.; Portehault, D. Structure-Activity Relationship in Manganese Perovskite Oxide Nanocrystals from Molten Salts for Efficient Oxygen Reduction Reaction Electrocatalysis. *Chem. Mater.* **2020**, *10.1021/ac*. https://doi.org/10.1021/acs.chemmater.0c00681.

(27) Gonell, F.; Alem, N.; Dunne, P.; Crochet, G.; Beaunier, P.; Méthivier, C.; Montero, D.; Laberty-Robert, C.; Doudin, B.; Portehault, D. Versatile Molten Salt Synthesis of Manganite Perovskite Oxide Nanocrystals and Their Magnetic Properties. *ChemNanoMat* **2019**, *5* (3), 358–363. https://doi.org/10.1002/cnma.201800632.

(28) Al Raihani, H.; Durand, B.; Chassagneux, F.; Kerridge, D. H.; Inman, D. Zirconia Formation by Reaction of Zirconium Sulfate in Molten Alkali-Metal Nitrates or Nitrites. *J. Mater. Chem.* **1994**, *4* (8), 1331. https://doi.org/10.1039/jm9940401331.

(29) Du, Y.; Inman, D. Reactions of Zr(SO4)2 in Molten Nitrite and Nitrate Systems. *J. Mater. Chem.* **1995**, *5* (11), 1927. https://doi.org/10.1039/jm9950501927.

(30) Du, Y.; Inman, D. The Acidic/Basic Effects on Preparation of Zirconia Powders from Molten Salts. *J. Mater. Sci.* **1996**, *31* (13), 5505–5511. https://doi.org/10.1007/BF00360735.

(31) Du, Y.; Inman, D. Synthesis of MgO Powders from Molten Salts. *J. Mater. Sci.* **1997**, *2*, 2373–2379.

(32) Jolivet, J.-P. *Metal Oxide Chemistry and Synthesis: From Solution to Solid State*; Wiley: Chichester, 2000.

(33) Deshmukh, R.; Niederberger, M. Mechanistic Aspects in the Formation, Growth and Surface Functionalization of Metal Oxide Nanoparticles in Organic Solvents. *Chem. - A Eur. J.* **2017**. https://doi.org/10.1002/chem.201605957.

(34) Afanasiev, P.; Geantet, C. Synthesis of Solid Materials in Molten Nitrates. *Coord. Chem. Rev.* **1998**, *178–180* (PART 2), 1725–1752. https://doi.org/10.1016/s0010-8545(98)00154-4.

(35) Cui, Z.; Wang, S.; Zhang, Y.; Cao, M. Engineering Hybrid between Nickel Oxide and Nickel Cobaltate to Achieve Exceptionally High Activity for Oxygen Reduction Reaction. *J. Power Sources* **2014**, *272*, 808–815. https://doi.org/10.1016/j.jpowsour.2014.08.097.

(36) Stoerzinger, K. a.; Lü, W.; Li, C.; Ariando; Venkatesan, T.; Shao-Horn, Y. Highly Active Epitaxial La(1–x)SrxMnO3 Surfaces for the Oxygen Reduction Reaction: Role of Charge Transfer. *J. Phys. Chem. Lett.* **2015**, *6*, 1435–1440. https://doi.org/10.1021/acs.jpclett.5b00439.

(37) Retuerto, M.; Pereira, A. G.; Pérez-Alonso, F. J.; Peña, M. A.; Fierro, J. L. G.; Alonso, J. A.; Fernández-Díaz, M. T.; Pascual, L.; Rojas, S. Structural Effects of

LaNiO3 as Electrocatalyst for the Oxygen Reduction Reaction. *Appl. Catal. B Environ.* **2017**, *203*, 363–371. https://doi.org/10.1016/j.apcatb.2016.10.016.

(38) Ji, Q.; Bi, L.; Zhang, J.; Cao, H.; Zhao, X. S. The Role of Oxygen Vacancies of ABO 3 Perovskite Oxides in the Oxygen Reduction Reaction. *Energy Environ. Sci.* **2020**, *13* (5), 1408–1428. https://doi.org/10.1039/D0EE00092B.

Table of contents